RSC Advances

PAPER

View Article Online
View Journal | View Issue

Check for updates

Cite this: *RSC Adv.*, 2018, **8**, 14936

A new mechanism for improving electromagnetic properties based on tunable crystallographic structures of FeCoNiSi$_x$Al$_{0.4}$ high entropy alloy powders†

Bin Zhang,[a] Yuping Duan, *[a] Yulong Cui,[a] Guojia Ma,[b] Tongmin Wang *[a] and Xinglong Dong [a]

Mechanical grinding method was employed to prepare FeCoNiSi$_x$Al$_{0.4}$ high entropy alloy powders, which present a simple solid solution structure (FCC and BCC). After annealing at 673 K, a large amount of BCC phase precipitate and a small amount of CoFe$_2$O$_4$ phase generate. The change of crystal structure may lead to an increase in M_s (from 100.3 emu g^{-1} to 124.2 emu g^{-1}) and a decrease in H_c (from 107 Oe to 59.5 Oe for FeCoNiSi$_{0.3}$Al$_{0.4}$). The silica content has a significant effect on the electromagnetic parameters of the as-milled and as-annealed alloy powders, presenting the trend of first increase and then decrease. And the dielectric constant is obviously improved after annealing (*e.g.* from 8.48 to 11.21 and from 0.15 to 2.84 for the ε' and ε'' of FeCoNiSi$_{0.3}$Al$_{0.4}$ at 18 GHz, respectively), while the permeability is reduced. Compared with those of the as-milled samples, the μ' of as-annealed FeCoNiSi$_x$Al$_{0.4}$ ($x = 0.1$, 0.3, 0.4) remain unchanged or even increase due to the formation of CoFe$_2$O$_4$. Meanwhile, the relative content of the precipitated BCC to FCC for FeCoNiSi$_{0.3}$Al$_{0.4}$ enhance with the annealing temperature increase from 573 K to 773 K, and then reduce. And the ε' and μ' at 2 GHz present the same trend as the content ratio ($A_{\text{BCC}}/A_{\text{FCC}}$), while the ε'' improve obviously after annealing, corresponding to the elevation of conductivity.

Received 28th February 2018
Accepted 8th April 2018

DOI: 10.1039/c8ra01762j

rsc.li/rsc-advances

1. Introduction

As the electronic devices using microwave frequency range are growing every single year, the hazards of electromagnetic (EM) wave on human body and equipment are increasing. To reduce or avoid the harms of EM wave, high-performance EM wave absorbing materials have high demand in civil, commercial and military applications, especially working under harsh conditions, such as oxidizing and corrosive conditions.[1–4] Meanwhile, the lightweight nanomaterials are the primary choice for EM wave absorbers.[5,6] Therefore, the high entropy alloy powders with the above merits are excepted to be a new generation of EM wave absorbing materials.

The high entropy alloys (HEAs) have received much attention in last ten years due to their high hardness and strength, outstanding wear resistance, good corrosion and oxidation resistance and combinations of two or more properties, which brings the new alloy design concept.[7–15] Different from traditional alloy, HEAs are defined as the alloys with five or more principal elements in equimolar or near-equimolar ratio and tend to form simple body-centered-cubic (BCC) and/or face-centered-cubic (FCC), and hexagonal close packed (HCP) solid solution due to the high configurational entropy.[16–21] In recent studies, some of the quaternary and ternary alloys in equimolar ratio are also considered as HEAs.[22–24]

Lin *et al.*[12] have proven that the corrosion potential and pitting potential of the FeCoNiCrAl$_{0.5}$ HEA in a 3.5 wt% NaCl solution are smaller than those of the AISI 304L stainless steel. Effects of Al element on the corrosion resistance behaviors of Fe$_{1.5}$Ni$_{0.5}$CrMnAl$_x$ HEAs were investigated, and it can be concluded that the pitting potentials of Al-containing alloys in NaCl solution are obviously lower than that of Al-free alloy.[25] These are because the surface of the alloy is easy to form an oxide film of Al$_2$O$_3$. Zhang *et al.*[26] have studied the high temperature oxidation properties of NbCrMoAl$_{0.5}$X (X = Ti, V, TiV, TiVSi$_{0.3}$). It proved that the addition of Al, Ti or Si element help to improve the oxidation resistance. Therefore, we can get that the HEAs with adding Si–Al elements have excellent corrosion resistance and high temperature oxidation resistance due to the presence of the "cocktail effects" for HEAs.

---

[a] *Key Laboratory of Solidification Control and Digital Preparation Technology (Liaoning Province), School of Materials Science and Engineering, Dalian University of Technology, Dalian 116085, P. R. China*

[b] *Beijing Aeronautical Manufacturing Technology Research Institute, Beijing 100024, PR China*

† Electronic supplementary information (ESI) available. See DOI: 10.1039/c8ra01762j

Recently, the magnetic properties of HEAs with varying composition have been extensively investigated. The CuAl contents had obvious influence on the microstructure and saturation magnetization of FeCoNi(CuAl)$_x$ alloy, and the M_s of FeCoNi(CuAl)$_{0.8}$ alloy increased from 78.9 Am^2 kg^{-1} to 93.1 Am^2 kg^{-1} by annealing at 673 K.[27] Annealing can effectively improve the saturation magnetization of a certain constituent. Zhang *et al.* have prepared the FeCoNi(SiAl)$_x$ HEAs by arc-melting method and found that the electrical resistivity increased and sacrificed the magnetization with adding SiAl content, and the coercivity with a single-phase structure (BCC or FCC) was smaller than that of the two-phase structure (BCC and FCC).[22] Therefore, the alloy components and annealing process have great influence on the magnetic properties of alloys. In addition, Chen *et al.* found that the electrical conductivity of FeCoNiCrAl$_x$ alloys decreased as x increasing in single-phase (FCC or BCC) regions and the electrical conductivity in duplex phase region possessed smaller value than that in single region.[14] It is clearly seen that the electrical conductivity is related to the composition and phase structure. As far as we know, Liu *et al.* have investigated the magnetic and EM wave absorbing properties of FeCoNiCrAl and FeCoNiCrAl$_{0.8}$ HEAs at different milling time. M_s ranges from 20.21 emu g^{-1} to 67.52 emu g^{-1}, while H_c distributes over an interval of 59.68 Oe to 142 Oe.[28,29]

Although a large number of literatures have studied the microstructures, mechanical and magnetic properties of HEAs, little attention have been paid to the effects of element content and annealing on the tunable crystallographic structures and relationship between crystal structures and EM properties of the high entropy alloy powders. In the paper, the quinary FeCoNiSi$_x$Al$_{0.4}$ HEA powders were prepared by mechanical alloying and processed by subsequent annealing treatment. The tunable crystallographic structures and EM properties of the alloy powders were investigated by adding different Si content. In addition, since the HEA powders can produce BCC and CoFe$_2$O$_4$ new phase after annealing, so effects of crystal structure on the magnetic and EM properties were studied. It is useful to modulate crystal structure and to optimize magnetic properties and EM parameters.

2. Experimental

2.1 Synthetic procedures

The elemental powders of Fe, Co, Ni, Si, and Al with purity higher than 99% and particle size less than 50 μm were used as raw materials. The HEA powders with nominal compositions of FeCoNiSi$_x$Al$_{0.4}$ (expressed in molar ratio, denoted as M$_x$, $x = 0.1$, 0.2, 0.3, 0.4, and 0.5) were prepared by mechanical milling for 70 h in a planetary ball mill (QM-QX4). A moderate amount of anhydrous ethanol as a process control agent was added into the reaction system before milling. The powder-to-ball (10 mm and 6 mm in diameter) weight ratio was 1 : 20, and the stainless steel pot rotation speed was 300 rpm. In addition, a pause of 4 min have been done to avoid excessive heating during milling, and the direction of the rotation was changed every half an hour. Then the alloy powders were annealed at 673 K, and denoted as A$_x$ ($x = 0.1$, 0.2, 0.3, 0.4, and 0.5).

2.2 Characterization

The phase composition of the prepared powders was tested by X-ray diffraction (XRD, Empyrean) using a Co K$_\alpha$ radiation (λ = 1.78901 Å) in the 2θ scan ranging from 30° to 120°, and the operating voltage and tube current was 35 kV and 50 mA. The morphology of the powders was performed by scanning electron microscopy (SEM, SUPRA55) with EDS. And the size distribution of alloy powders were measured by laser scattering particle size distribution analyzer (LA960WET). The magnetic properties of the alloy powders were measured with vibrating sample magnetometer (VSM7404) with a maximum applied field of 10 000 Oe at room temperature. The electrical conductivity was measured using four point probe measurement (RTS-9), and the cylinders used for measurement were cold pressed by presses at 10 MPa. The complex permittivity ($\varepsilon(f)$) and permeability ($\mu(f)$) were measured by Agilent vector network analyzer (8720B) in the frequency of ranging of 2–18 GHz. The mixture used for EM parameter measurements were prepared by blending the milled powers and paraffin at weight ratio of 6 : 4, and then a concentric cylinder with 3.00 mm in inner diameter, 7.00 mm in outer diameter and 2.00 mm in thickness was prepared by using a mold.

3. Results and discussion

3.1 Structural characterization

Fig. 1(a) shows the XRD patterns of as-milled FeCoNiSi$_x$Al$_{0.4}$ alloy powders with varying Si content. It is distinct that all alloy powders are composed of a large amount of FCC phase (corresponding to (111), (200), (220) crystal face) and a small amount of BCC phase (corresponding to (110), (200), (211) crystal face), indicating the formation of complete solid solution (high entropy alloy). The diffraction peaks of BCC phase are obscure and even no peak of the (110) crystal face is observed, which could be due to the low content and the relatively low diffraction intensity.[30–32] The peaks of Si at around 33.2° and 55.5° can be indexed as the (111) and (220) diffraction planes of Si (JCPDS, no. 27-1402), respectively. Si is incomplete dissolution because Si has a diamond-type crystal structure that is different from other elements. And the dissolution rate of the element is related to the melting point and crystal structure, and the elements with low melting point and the same crystal structure are more soluble. In addition, the structure of diamond-type is more difficult to break up, which is the another reason for Si failed to dissolve. The insertion shows an enlarged picture of the main peaks of FCC phase. Because of the lattice parameter of FCC phases decrease slightly by adding Si element with smaller atomic radius, the peaks are shifted rightwards. In addition, the relative XRD intensity of FCC phase reduce along with the increase of Si content. This is because the augment of the X-ray diffusive scattering effect, and this phenomenon is the result of the larger lattice distortion caused by the atomic radius's difference between the adding atoms and inherent atoms.

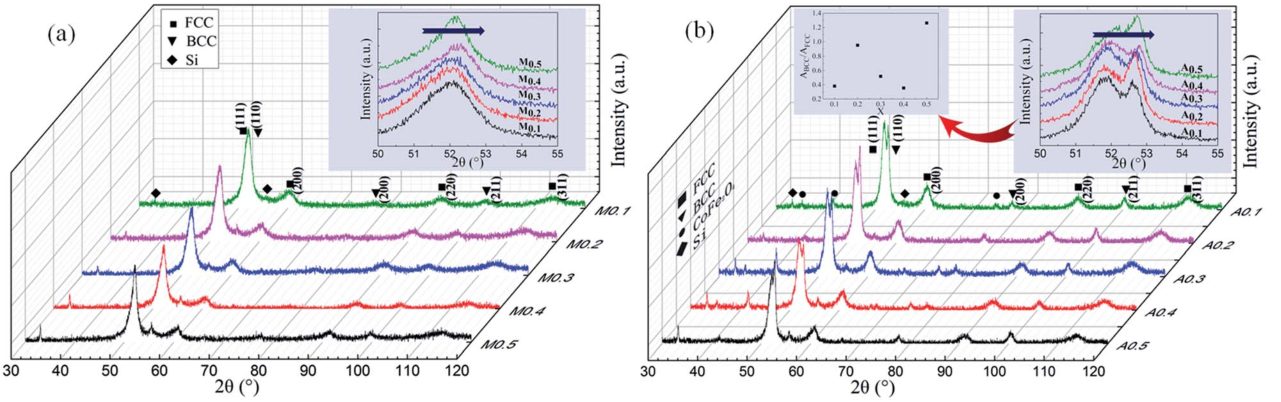

Fig. 1 XRD patterns of (a) as-milled and (b) as-annealed FeCoNiSi$_x$Al$_{0.4}$ HEA powders, and the detailed scans in the range of $2\theta = 50$–$55°$ are presented in the illustration. The change in area ratio (A_{BCC}/A_{FCC}) for the as-annealed HEA powders is also presented in the illustration. All alloys are composed of BCC and FCC phase except a small amount of Si remained indicating the formation of high entropy alloy.

Such a phenomenon is not uncommon for HEAs system, and it also presents in other HEAs system.[10,14] For example, the relative intensity of main peak decreases with increasing Al addition in FeCoNiCrAl$_x$ alloys.

Fig. 1(b) shows the XRD patterns of as-annealed FeCoNiSi$_x$-Al$_{0.4}$ alloy powders with varying Si content. The crystal structures are same with those of milled alloy powders. Differently, the intensity of the Si peaks at 33.2° and 55.5° decrease and this is because the silicon gradually dissolves in the matrix after annealing. And the intensity of the diffraction peaks magnify, on account of the increase in crystallinity and crystallite size and the decrease in internal stress of the alloy powders. The illustration shows an enlarged picture of peak positions at $2\theta = 50$–$55°$. The offset direction is similar with that of the milled powders. In addition, the diffraction peaks located at 2θ of 52.7° and 41.53° appear after annealing, indicating that BCC alloy phases precipitate and the CoFe$_2$O$_4$ (JCPDS, no. 22-1086) phases generate. And the size of the CoFe$_2$O$_4$ phase for samples A$_{0.1}$, A$_{0.3}$, A$_{0.4}$ are larger than others. Moreover, the relative content of BCC to FCC (ratio of the integral area, A_{BCC}/A_{FCC}) for the as-annealed powders are presented in the illustration.

3.2 Microscopic characterization

The morphologies and particle sizes of different samples are characterized using SEM. Fig. 2(a–e) presents the back-scattered images of the as-annealed FeCoNiSi$_x$Al$_{0.4}$ alloy powders with varying Si content. The sizes of the particles present a uneven distribution, varying from hundreds of nanometers to hundreds of micrometers. All of the alloy particles present an aggregation composed of elliptic ball shape (see Fig. 2(f)) for using alcohol as grinding media, which leads to the aspect ratio increase and results in the decline of eddy current loss and the acclivity of surface polarization simultaneously.[33–36] It can be seen that the morphologies of all alloy particles are similar and the particle size distribution are inhomogeneous. So the size distribution of as-milled and as-annealed alloy powders were measured by laser particle size distribution analyzer, as shown in Fig. 2(o and p). After annealing, the particle sizes are obviously increased by the aggregation of small particles. Roughly, the sizes of the as-milled particles present an uptrend with the increase of Si content and then decline. However, the

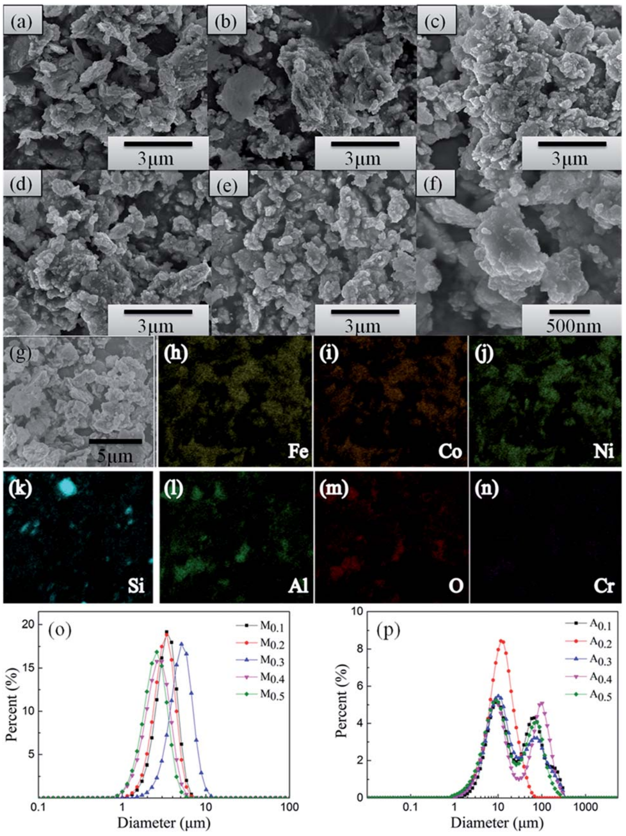

Fig. 2 SEM backscattering electron images of FeCoNiSi$_x$Al$_{0.4}$ HEA powders: (a–e) A$_{0.1–0.5}$, and (f) an enlarged figure of the A$_{0.3}$ alloy particles. All alloy powders present an aggregation composed of elliptic ball shape. Elements mapping of (h) Fe, (i) Co, (j) Ni, (k) Si, (l) Al, (m) O, and (n) Cr for (g) as-annealed A$_{0.3}$ alloy powders. Size distribution of (o) as-milled and (p) as-annealed alloy powders in different Si content, and the aggregation of diminutive particles generate larger particles after annealing.

size distribution in Fig. 2(p) is abnormally due to the irregular aggregation of particles during the annealing process. Fig. 2(g–n) show the elemental mapping of Fe, Co, Ni, Si, Al, O, and Cr for sample $A_{0.3}$. Among them, the elements of O and Cr are introduced into system during the ball milling. It is evident that the other five elements are dispersed better and there is the presence of undissolved silicon element. This is corresponding to the result of XRD. Besides, the oxidation of the particles' surface is inevitable.

The TEM (a and e) and HRTEM (b and f) images of the as-milled (a–c) and as-annealed (d–h) $FeCoNiSi_{0.3}Al_{0.4}$ HEA powders are presented in Fig. 3. As depicted in the bright field image (Fig. 3(a) and (e)), the smaller particles of both HEA powders also present elliptic ball shape. The interplanar *d* spacings of 0.20 nm and 0.21 nm could be obviously observed in the HRTEM image, which are consistent with the (110) and (111) crystallographic planes of the BCC and FCC phase, respectively. Moreover, the newly generated $CoFe_2O_4$ phase can be observed from HRTEM and SAD, which is in agreement with the XRD dates. Obviously, various crystalline structures are surrounded by amorphous structure, and the boundaries between crystal and amorphous phases become more pronounced after annealing. From the SAD, it can be seen that more amorphous phase are contained in the milled sample and many crystal diffraction spots are generated after annealing. This illustrates that the crystallinity rise after annealing.

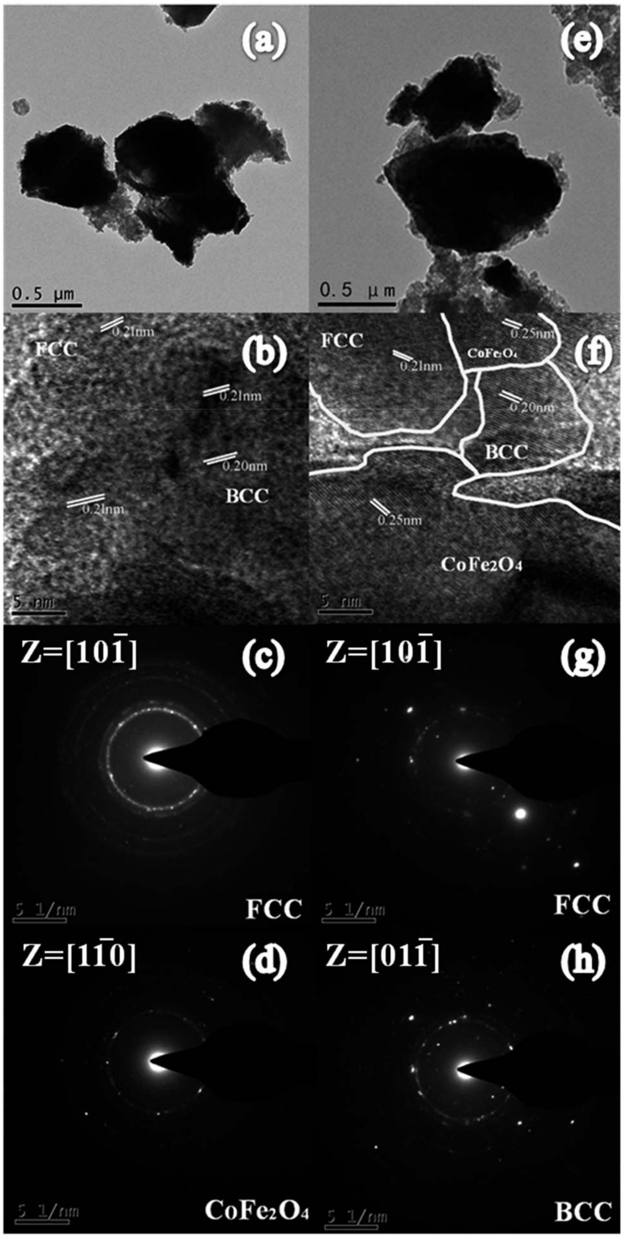

Fig. 3 (a and e) TEM and (b and f) HRTEM images of (a–c) as-milled and (d–h) as-annealed $FeCoNiSi_{0.3}Al_{0.4}$ HEA powders. The SAED patterns (c) and (d, g and h) for the samples.

3.3 Magnetic properties

Fig. 4 displays the hysteresis loops of (a) $M_{0.1-0.5}$ and (b) $A_{0.1-0.5}$ alloy powders measured at room temperature with an applied field of −10 000 Oe to 10 000 Oe. It is obvious that all alloy powders present partial soft magnetic peculiarity. Compared with the FeCoNiCrAl HEA powders, all alloy powders possess biggish saturation magnetization, which may lead to a higher initial permeability.[28,29] The coercivity (H_c) and saturation magnetization (M_s) of $FeCoNiSi_xAl_{0.4}$ as a function of Si content are given in the inset. In Fig. 4(a), the M_s decreases from 104.1 emu g^{-1} to 89.5 emu g^{-1} and the H_c increases from 91.3 Oe to 148.8 Oe. Adversely, the M_s of $A_{0.3}$ has the maximum value (124 emu g^{-1}) and declines in other concentrations, while the H_c presents an enlarging trend within the whole range with a deviation in $A_{0.3}$ in Fig. 4(b).

In the light of the fact that the M_s is primarily determined by the composition and atomic-level structure, and the H_c is sensitive to the grain size, impurity, and the heat-treatment process.[22] So, the reason for the M_s decrease with the increment of Si content is more 3d electrons of magnetic atoms transfer to the 2p electron layer of Si atoms, while the augment in H_c is due to the ineradicable point defect rise, corresponding to the Si content increase. After annealing, the M_s and H_c of the alloy powders with same Si content rise. The M_s increase is attributed to the precipitation of the BCC phase, and the magnitude of ΔM_s (M_s (A_x) − M_s (M_x)) is related to the relative content of the precipitated BCC to FCC (A_{BCC}/A_{FCC}). Although the stress and defects generated in the process of milling are reduced after annealing, the increase in magnetic anisotropy constant (K_1), magnetostriction coefficient (λ_s), crystallinity, crystallite size (D), particle size and M_s can magnify magnetic anisotropy, stress anisotropy and shape anisotropy, which bring about the increase of H_c. The anomalies of ΔM_s and ΔH_c (H_c (A_x) − H_c (M_x)) for $A_{0.1}$, $A_{0.3}$ and $A_{0.4}$ attribute to the generation of new phase $CoFe_2O_4$ (in Fig. 4(c and d)). Namely, the $CoFe_2O_4$ phase can effectively improve M_s and lower H_c. The analysis of magnetic properties are corresponding to the test results of XRD.

3.4 EM parameters analysis

For microwave absorbing materials, the relative complex permittivity ($\varepsilon_r = \varepsilon' - j\varepsilon''$) and the relative complex permeability

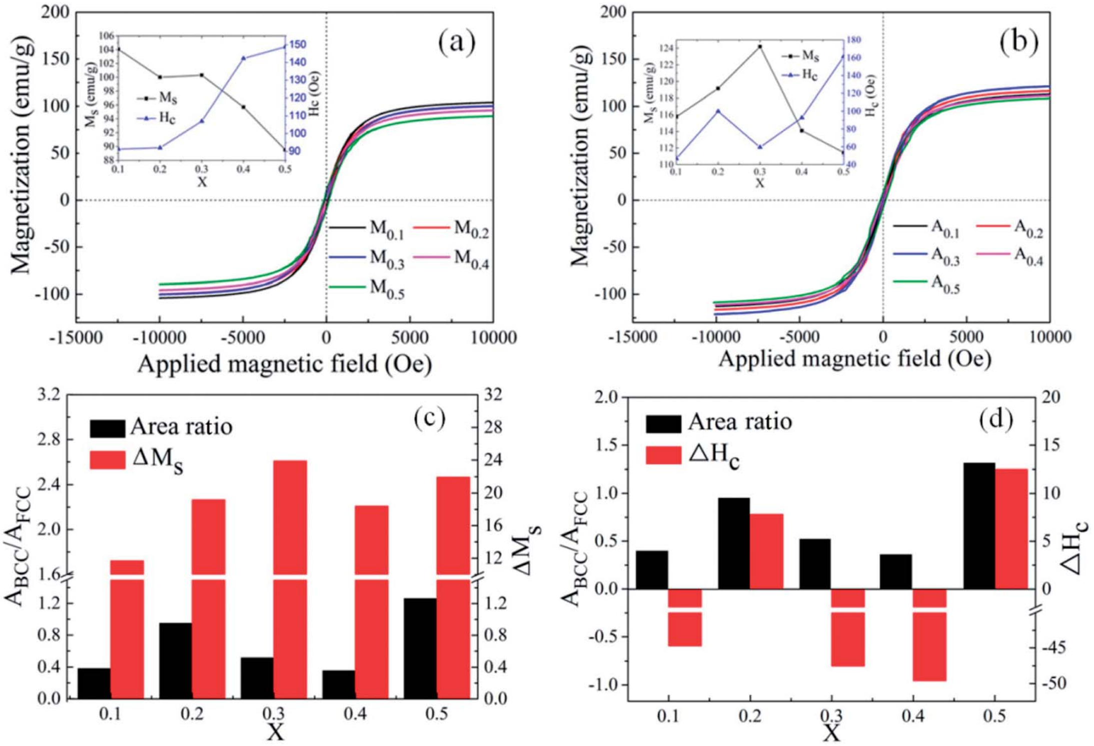

Fig. 4 Hysteresis loops of (a) $M_{0.1-0.5}$ and (b) $A_{0.1-0.5}$, and the illustrations present the change in magnetic parameters (H_c and M_s) of both kinds of alloy powders. (c–d) is the area ratio (A_{BCC}/A_{FCC}), ΔM_s (M_s (A_x) $-$ M_s (M_x)), and ΔH_c (H_c (A_x) $-$ H_c (M_x)) for different alloy powders. Wherein X represents the molar amount of Si in $FeCoNiSi_xAl_{0.4}$ alloy powders.

($\mu_r = \mu' - j\mu''$) are the key point to determine the absorbing properties. Generally, the real parts (ε' and μ') and the imaginary parts (ε'' and μ'') represent the energy storage and energy dissipation respectively. The energy is stored through dipole displacement polarization and resonance when the EM wave radiates to the surface of the absorbing materials. And the energy is dissipated by the way of conduction loss, dielectric loss and magnetic loss.

Fig. 5 shows the frequency dependence of (a and e) the real parts (ε') and (b and f) the imaginary parts (ε'') of complex permittivity of (a and b) as-milled and (e and f) as-annealed (at 673 K) alloy powders within the range of 2–18 GHz. The ε' of all alloy powders change a little in the 2–18 GHz range, and the ε'' of as-annealed powders gradually rise with the increment of frequency. It is apparent that the Si contents have a strong impact on the permittivity of both kinds of alloy powders. The ε' of alloy powders $M_{0.1-0.5}$ increase from $M_{0.1}$ ($\approx$6.8) to $M_{0.3}$ ($\approx$8.5) along with the Si content increasing and get the maximum value at $M_{0.3}$, and then decrease to $M_{0.5}$ ($\approx$7.5). And the change of ε'' (in the frequency range of 2–10 GHz) along with Si content agrees with that of ε'. The increase in dielectric constant can be illustrated by the following three reasons. Firstly, the polarization sites have a positive correlation with the point defects, and as the increase of Si content induce more point defects, which results in the growth of polarization effect. Secondly, while at a relatively lower content ($x \leq 0.3$), the surface polarization rises with the enlargement of aspect ratio, corresponding to the increase of Si content (see Fig. 2(o)). Finally, the skin depth presents an uptrend with the increment of electrical resistivity. Previous researches show that only part of magnetic materials within the skin depth interact with the EM wave.[37] The larger the skin depth is, the more fraction of magnetic materials absorbing the EM wave is. The decrease of dielectric constant can be explained by the following reasons similarly. Compared with the metal elements, the brittleness of Si element is larger. While at a relatively higher content ($x \geq 0.4$), the surface polarization weakening caused by the reduction of aspect ratio gives rise to the decrease of permittivity. Moreover, researches demonstrate a negative correlation between the interaction radius of dipole and the point defects when the defects are more, and as the smaller radius induce the less displacement polarization.[38] Furthermore, the electrical resistivity ($\rho = 1/\sigma$) increase results in the decline of ε' and ε'' (conduction loss) directly, according to the formulas Debye's relaxation:[39]

$$\varepsilon' = \sigma/\omega^2\tau\varepsilon_0 + \varepsilon_\infty \tag{1}$$

$$\varepsilon'' = \sigma/\omega\varepsilon_0 \tag{2}$$

where ω ($\omega = 2\pi f$) is the angular frequency, τ is the relaxation time of dipoles, ε_0 and ε_∞ are the permittivity at static frequency and at infinite frequency, respectively.

Compared with the as-milled samples, the as-annealed samples possess a larger dielectric constant value. The most fundamental reason is the decrease in defects, the formation of $CoFe_2O_4$ and BCC (FeCo) phase and the growth of particles from

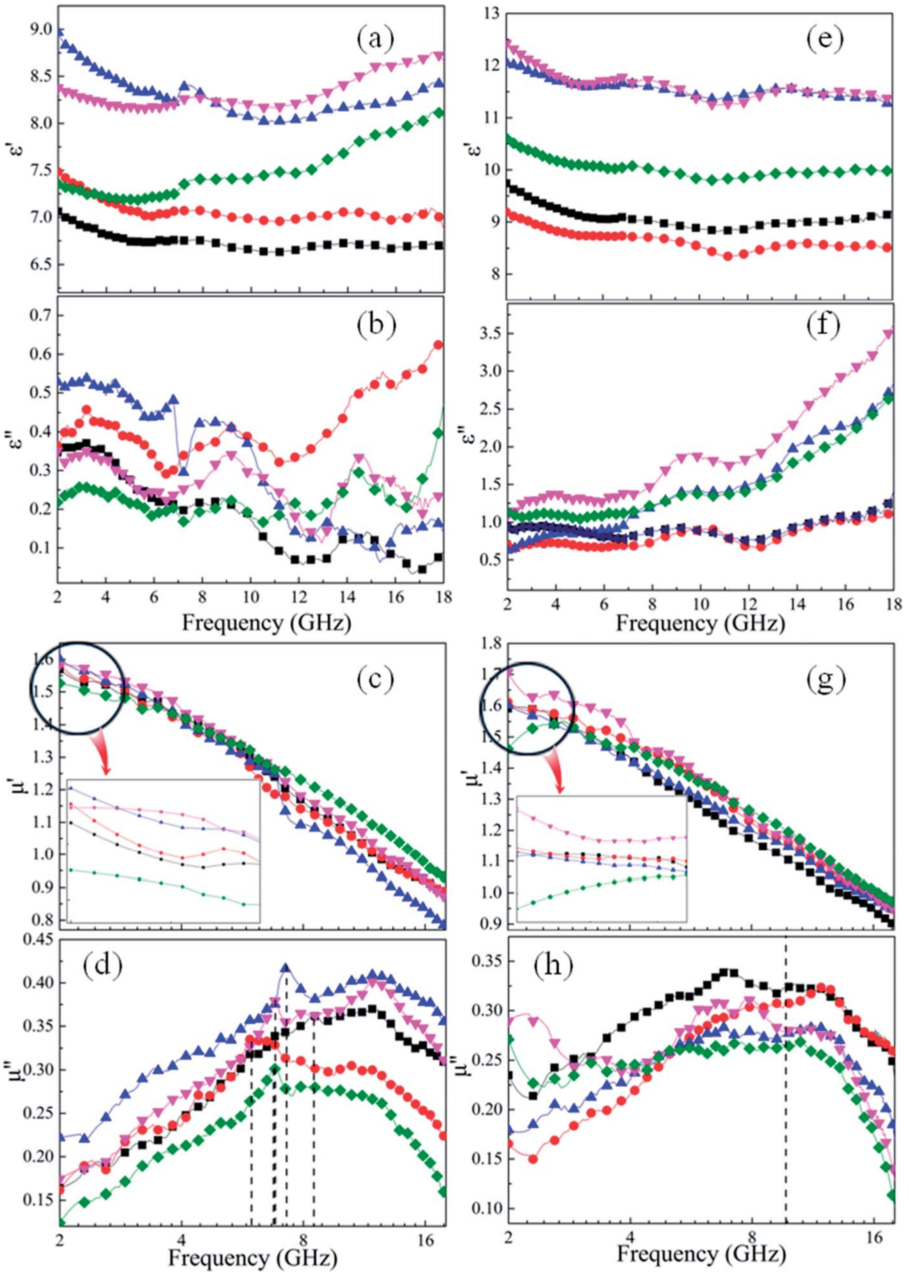

Fig. 5 Frequency dependence of (a and e) ε', (b and f) ε'', (c and g) μ', and (d and h) μ'' for the (a–d) as-milled and (e–h) as-annealed FeCoNiSi$_x$Al$_{0.4}$–paraffin composites. The symbols of ■, ●, ▲, ▼ and ◆ denote the $x = 0.1$, 0.2, 0.3, 0.4, and 0.5 composites, respectively.

the process of annealing. First of all, the interaction radius of dipole presents an uptrend with the reduction of defects, and then the displacement polarization could be increased, which leads to the enlargement of ε'. At the same time, an increase in phase-interface caused by the formation of $CoFe_2O_4$ and BCC phase induces the enhancement of interfacial polarization. And the growth of particles results in the increase of surface polarization. The ε' of the alloy powders $A_{0.2}$ ($\approx$8.6) and $A_{0.4}$ ($\approx$11.7) does not conform to the original change rule of the as-milled powders. This may be caused by the particle sizes are different from other samples. The sample $A_{0.2}$ has smaller particle, and the sample $A_{0.4}$ has larger particles than other alloy powders (see Fig. 2(p)). Meanwhile, the augment of electrical conductivity (see Fig. 6(a)) caused by the decrease of defects brings about the augment of ε' and ε'' (according to the eqn (1) and (2)), especially in the high frequency area. And the magnitude of $\Delta\varepsilon''$ (ε'' (A_x) − ε'' (M_x)) at high frequency for $A_{0.1}$, $A_{0.3}$, and $A_{0.5}$ agree well with the increment of conductivity ($\Delta\sigma$) (in Fig. 6(b)). To the sample $A_{0.2}$, the polarization loss is less than others due to the generation of smaller particles, which leads to the smaller increase of ε'', and the opposite is true for the sample $A_{0.4}$. Namely, the ε'' in high frequency is mainly the role of conductive loss. And the enlargement of conductivity can be illustrated by the formula of the metallic resistivity:

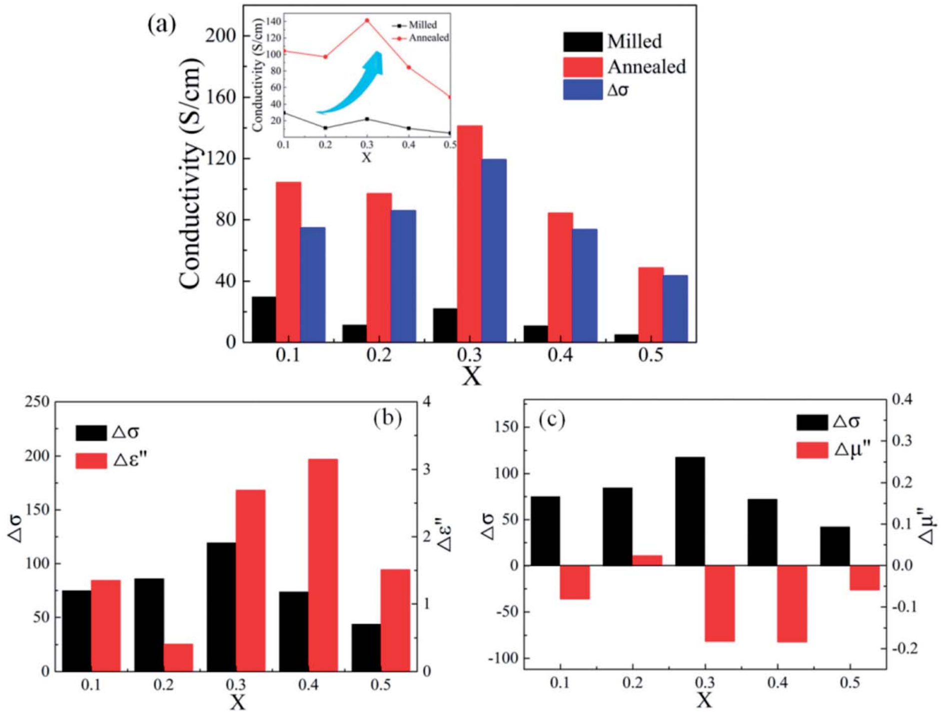

Fig. 6 (a) The change in the conductivity of as-milled, as-annealed alloy powders and the increment ($\Delta\sigma$) are presented. (b andc) is the $\Delta\sigma$, $\Delta\varepsilon''$ (at 18 GHz), and $\Delta\mu''$ (at 10 GHz) for different alloy powders. Wherein X represents the molar amount of Si in FeCoNiSi$_x$Al$_{0.4}$ alloy powders.

$$\rho = \frac{m}{ne^2}\left(\frac{1}{\tau_T} + \frac{1}{\tau_R}\right) \tag{3}$$

where m, n, e, τ_T, and τ_R present the quality, the density, the charge of free electrons, and the scattering relaxation times caused by the lattice thermal vibration and the lattice defects, respectively. The augment of scattering relaxation time caused by the decreased defects diminishes the resistivity, corresponding to magnifying the conductivity. It can be seen that the change of ε'' is the same as that of ε', roughly. This can be explained by the formula of Debye's relaxation: $\varepsilon' = \varepsilon''/\omega t + \varepsilon_\infty$. The ε'' is proportional to the ε'. It is worth mentioning that the conductivity of $A_{0.3}$ is higher than that of $A_{0.2}$, and the same phenomenon can be found in FeCoNi(SiAl)$_x$ alloys.[22]

Fig. 5 shows the frequency response of (c and g) the real parts (μ') and (d and h) the imaginary parts (μ'') of complex permeability of (c and d) as-milled and (g and h) as-annealed (at 673 K) alloy powders within the 2–18 GHz range. As shown in Fig. 5(c and d), the μ' decrease gradually and stabilize in the high frequency, and the μ'' present an open downward parabolic shape over the almost entire frequency range, which is caused by the inhomogeneity of the particle size distribution (see Fig. 2(o)).[40] Similar to the change of the complex permittivity, the μ' of alloy powders $M_{0.1-0.5}$ at 2 GHz increase from $M_{0.1}$ (1.57) to $M_{0.3}$ (1.60) along with the increase of Si content and get the maximum value at $M_{0.3}$, and then decrease to $M_{0.5}$ (1.52). It can be explained by the empirical formula of the initial permeability (μ_i):[41]

$$\mu_i \approx \frac{\mu_0 {M_s}^2}{\left(K_1 + \frac{3}{2}\lambda_s\sigma\right)\beta^{1/3}\frac{\delta}{d}} \tag{4}$$

where M_s, K_1, λ_s, σ, β, δ and d present the saturation magnetization, the magnetocrystalline anisotropy constant, the magnetostrictive coefficient constant, the internal strain, the volume concentration of impurity, the domain wall thickness and the impurity diameter, respectively. It is apparent that a positive correlation between M_s and μ_i can be seen from the formula, while K_1, λ_s, σ and β is negatively correlated with μ_i. The M_s, K_1 and λ_s decrease with the Si content increasing from $x = 0.1$ to $x = 0.3$. The combination of these three factors enhance the permeability, and the increment is smaller because of the opposite effect between M_s and K_1, λ_s. Instead, the reduction in permeability can be explained by the following three reasons. First, the decreased M_s and the increased K_1 and λ_s bring down the permeability. The values of K_1 and λ_s close to zero when $x \approx 0.3$. Second, the exchange coupling reaction of the magnetic moments between particles weakens as the surface area minishes, resulting in the increase of K_1 and decrease of μ_i.[42,43] Third, the increase of σ and β can also reduce μ_i. These changing rules can be illustrated by the shape-dependent Snoek's law similarly and it's formula is showed here:

$$\mu_i - 1 = 4\pi M_s/(H_k + 4\pi M_s N_h) \tag{5}$$

where H_k and N_h present the magnetocrystalline anisotropy energy and the demagnetization factor in the direction of width, respectively. The denominator represents the total anisotropy energy and $4\pi M_s N_h$ represents the shape anisotropy energy.[40] Similar to the effect of K_1, the H_k decreases to zero and then increases along with the Si content increasing. The combination effect of M_s and H_k results in the change of μ_i.

The imaginary parts (μ'') of complex permeability possess a wide resonance peak over the whole frequency range. The changing trend of μ'' is consistent with that of μ', and this can be illustrated by the formula of eddy current loss. Formula is expressed as follows:

$$\mu_r'' = 3\pi\mu_0(\mu')^2 d^2 f\sigma \tag{6}$$

It is clearly that μ_r'' is proportional to μ' and conductivity (σ). So the value of μ_r'' increases firstly and then decreases. To recognize carefully, the location of resonance peaks agree with the distributions of particles. This can be illustrated by the formula of natural resonance or shape-dependent Snoek's limit. According to the natural resonance frequency equation,

$$2\pi f_r = \gamma H_a \tag{7}$$

the anisotropy energy (H_a) declination caused by the aspect ratio reduction leads to the frequency of natural resonance (f_r) decrease. This changing role can be illustrated similarly by the shape-dependent Snoek's limit and it's formula is showed here:

$$(\mu_i - 1)f_r^2 = (\gamma/2\pi)^2 4\pi M_s(H_k + 4\pi M_s N_\perp) \tag{8}$$

$$N_h = \frac{1 - N_\perp}{2} \tag{9}$$

where γ and $N_\perp$ present the gyromagnetic ratio and the demagnetization factor in the direction of thickness, respectively.[33,40] N_h and $N_\perp$ are a function of aspect ratios and the larger flakes have smaller N_h values. It is easy to understand that the f_r agrees with particle size distribution.

Compared with those of the as-milled alloy powders, the μ' of the $A_{0.1}$, $A_{0.3}$, $A_{0.4}$ samples get larger and the $A_{0.2}$ and $A_{0.5}$ get smaller, ranging from 1.46 ($A_{0.5}$) to 1.70 ($A_{0.4}$) (see Fig. 5(g and h)). The reason for this phenomenon is the BCC (FeCo) phase precipitate out after annealing, and Fe and SiAl elements are separated from each other. The M_s, K_1 and λ_s for the as-annealed powders increase at the same time and the increment of M_s for $A_{0.1}$, $A_{0.3}$, $A_{0.4}$ is larger than others, corresponding to the formation of $CoFe_2O_4$ phase, which result in the diversification. In addition, the decrease in σ and β caused by annealing bring about the amplify of μ' according to the eqn (4), which prompt the enlargement of μ'. Moreover, these three samples possessing larger values of $\Delta\mu'$ (μ' (A_x) − μ' (M_x)) have smaller ΔH_c. On account of the skin depth reduction caused by the enlargement of conductivity and particle sizes, the μ'' of the as-annealed samples become smaller. And the magnitude of $\Delta\mu''$ (μ'' (A_x) − μ'' (M_x)) for $A_{0.1}$, $A_{0.3}$, and $A_{0.5}$ agree with the increment of conductivity ($\Delta\sigma$) (in Fig. 6(c)). To the sample $A_{0.2}$, the particle size turns into smaller than the skin depth, which leads to the larger $\Delta\mu''$, and the opposite is true for the sample $A_{0.4}$. In addition, the resonance peaks disappear after annealing, which is caused by the extreme non-uniformity of the particles (see Fig. 2(p)).

Based on these results, we propose the change of crystal structure for $FeCoNiSi_xAl_{0.4}$ system in the process of milling and annealing and the interaction mechanism with EM wave as a consistent explanation of all the above experimental observations as depicted in Fig. 7. The initial powders of Fe, Co, Ni, Si, and Al possess the crystal structure with BCC, HCP, FCC, CDT (cubic diamond type), and FCC phase, respectively. The

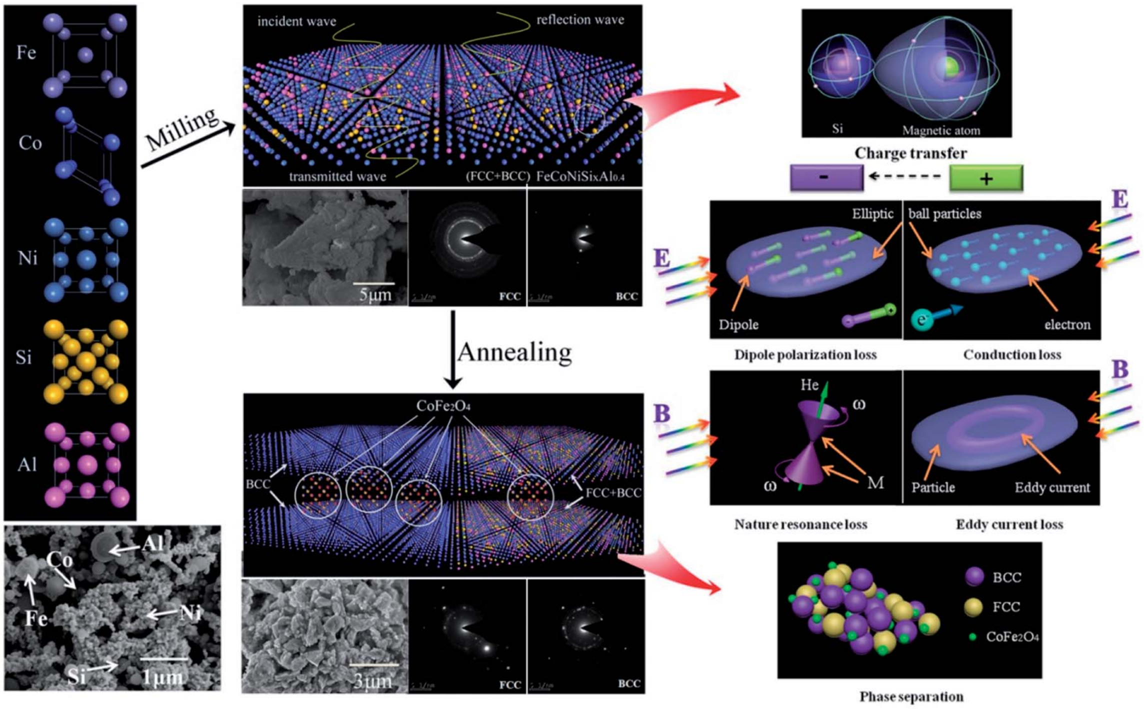

Fig. 7 Schematic illustration of the change of crystal structure in the process of milling and annealing and the mechanism interacted with EM wave for HEA powders.

FeCoNiSi$_x$Al$_{0.4}$ alloy powders with FCC and BCC phase crystal structure were prepared by the process of ball milling, where, all the elements are mixed together randomly. The alloy powders show elliptic ball shape because of the use of alcohol as a control agent.

For the milled alloy powders, Si element are evenly distributed around the magnetic elements, and the charge flows from magnetic atoms into the silicon atom, which brings about the M_s decrease and a microstructural asymmetry generation, and results in the formation of a permanent electric dipole that can excite a dipole polarization under the alternating EM field. When the EM wave irradiate to the particle surface, the EM field will generate the electric and magnetic field component in the direction of paralleling to the surface of particles. The alternating electrical field interact with the alloy material to create conduction loss. Meanwhile, the alloy particles will be magnetized under the alternating magnetic field to generate the magnetization (M). The compound interaction of magnetocrystalline, shape and stress anisotropy field produce a valid field (H_e), which can replace the extra steady magnetic field and interact with M, then generate nature resonance when satisfies the formula $2\pi f = \gamma H_e$. In addition, a kind of ring induction current, known as eddy current, are generated in the direction of perpendicular to the magnetic flux, which can induce the eddy current loss. All of the above types can attenuate the EM wave.

After annealing, the FeCo and CoFe$_2$O$_4$ phase respective with BCC phase and spinel crystal structure are separated out from the matrix, which give rise to the increase in interface (phase interface and particle surface) polarization. And the decrease of defects magnify the conduction loss. Meanwhile, the clutter distribution of anisotropy caused by the phase dissociation leads to the clutter distribution of valid field, which result in the resonance peak disappear. And the size of the reunited alloy powders are larger than that of the reduced skin depth, which bring about the reduction of the effective volume for the alloy powders interacted with EM wave.

To further investigate the variations of EM parameters with the annealing temperature, the XRD and EM parameters of as-annealed (at 573–873 K) FeCoNiSi$_{0.3}$Al$_{0.4}$ alloy powders were tested.

XRD patterns of the as-milled and as-annealed FeCoNiSi$_{0.3}$Al$_{0.4}$ alloy powders are shown in Fig. 8. Along with the annealing temperature rises, the intensity of (111), (200) and (220) for FCC increase, which attribute to the augment of crystallinity, while BCC (corresponding to (110), (200) and (211) crystal face) begin to precipitate at 673 K and get the maximum value at 773 K, and then decrease. In addition, the new phase CoFe$_2$O$_4$ starts to generate at 673 K and its magnitude gets down with the annealing temperature increasing. The insect shows an enlarged picture of the main peaks of FCC and BCC phase. Obviously, the peaks shift leftwards slightly due to the increase in the lattice parameter of the FCC phase. It can be illustrated that the Si element dissolves into the alloy phase gradually during the annealing process. And the intensity of 33.2° for silicon peak is reduced by degrees. Meanwhile, the relative content of BCC to FCC (A_{BCC}/A_{FCC}) for the as-annealed powders at different temperatures are presented in the illustration, and it shows a tendency to increase first (from 573 K to 773 K) and then to decrease.

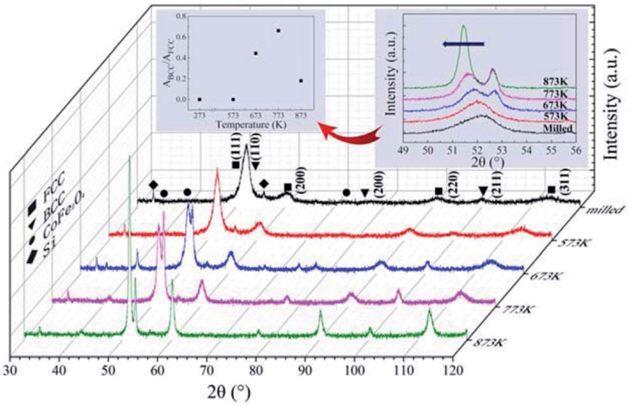

Fig. 8 XRD patterns of the as-milled and as-annealed (573–873 K) FeCoNiSi$_{0.3}$Al$_{0.4}$ alloy powders, and the inset present the detailed scans in the range of $2\theta = 49–56°$. The relative content of BCC to FCC (A_{BCC}/A_{FCC}) for different anneal temperature are also presented in the illustration.

Fig. 9 shows effects of the annealing temperature on the (a) ε' (b) ε'' (c) μ', and (d) μ'' for the as-annealed (at 573–873 K) FeCoNiSi$_{0.3}$Al$_{0.4}$ alloy powders. The ε' presents an uptrend with the increase of annealing temperature and reaches a maximum at 773 K, and then decreases. This may be caused by the relative content of BCC to FCC (in Fig. 8), since the growth of these two phases interface can store more energy. The effects of annealing temperature on ε'' are obvious, especially in high frequency area, and the increment of ε'' depends on the increment of conductivity (in Fig. 10). This is also true that the conduction loss play a major role in the high frequency range. The annealed sample (at 773 K), possessing larger interfacial polarization and loss, get a greater increase in ε'' than other samples. After annealing, the μ' at 2 GHz decrease first and then increase (from

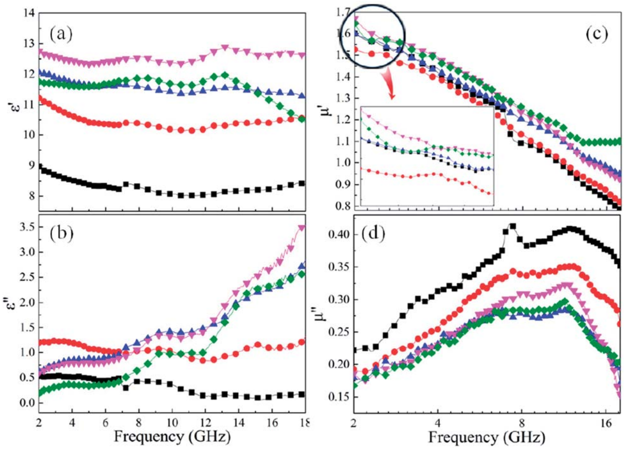

Fig. 9 Frequency dependence of (a) ε', (b) ε'', (c) μ', and (d) μ'' for the as-annealed (573–873 K) FeCoNiSi$_{0.3}$Al$_{0.4}$–paraffin composites. The symbols of ■, ●, ▲, ▼ and ◆ denote the milled, 573 K, 673 K, 773 K and 873 K composites, respectively.

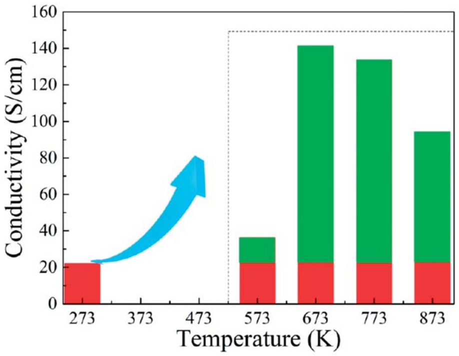

Fig. 10 Effect of annealing temperature on the conductivity of $FeCoNiSi_{0.3}Al_{0.4}$ alloy powders.

573 K to 773 K), which is the combination effect of M_s, K_1 and λ_s, and the decrease in μ'' may be caused by the fact that the particle size turn into larger than the skin depth, similarly.

The reflection loss of the as-milled and as-annealed (673 K) $FeCoNiSi_xAl_{0.4}$ ($x = 0.1$, 0.2, 0.3, 0.4, and 0.5) alloy powders and the EM parameters of as-annealed (573–873 K) $FeCoNiSi_xAl_{0.4}$ ($x = 0.1$, 0.2, 0.4, and 0.5) alloy powders are presented in the supporting.

4. Conclusions

$FeCoNiSi_xAl_{0.4}$ HEA powders are prepared by mechanical ball milling and processed by annealing (at 673 K), and the relation between Si content, microstructure and magnetic and EM properties are investigated. The M_s decrease and the H_c increase with the increase of Si content for the as-milled samples and the M_s and H_c rise after annealing. The $CoFe_2O_4$ phase generated in the annealing process has a beneficial to magnify M_s and diminish H_c. The ε' of the as-milled alloy powders rise first along with the Si content increase, then reduce, and has a maximum value, $\varepsilon' \approx 8.5$ ($M_{0.3}$). The μ' present the same changing rule, and get the maximum value at $M_{0.3}$ (1.60 at 2 GHz). After annealing, the ε' and ε'' have an obviously increase, while the μ'' decrease. The generation of $CoFe_2O_4$ phase can magnify μ'. The conductivity has been significantly improved after annealing, and the ε'' in high frequency is mainly the role of conductive loss. Moreover, the annealing temperature has a significant impact on the relative content of $CoFe_2O_4$ and the precipitated BCC to FCC, and the change of EM parameters agree with this transformation.

Conflicts of interest

There are no conflicts to declare.

Acknowledgements

The authors acknowledge the supported by Program for the National Key R&D Program of China (2017YFB0703103), the National Natural Science Foundation of China (No. 51577021, U1704253), the Fundamental Research Funds for the Central Universities (DUT17GF107), the Industry-University-Research Collaboration Project of Aviation Industry Corporation of China (cxy2103DLLG34).

Notes and references

1 Y. Z. Shi, B. Yang and K. L. Peter, *Metals*, 2017, **7**, 43.
2 X. M. Liu, Z. J. Yu, R. Ishikawa, L. Q. Chen, X. F. Liu, X. W. Yin, Y. C. Ikuhara and R. Riedel, *Acta Mater.*, 2017, **130**, 83–93.
3 Z. Guo, S. E. Lee, H. Kim, S. Park, H. T. Hahn, A. B. Karki and D. P. Young, *Acta Mater.*, 2009, **57**, 267–277.
4 S. S. Zuo, H. X. Bai, Q. Han, H. G. Liao, H. B. Gu and Z. F. Chen, *Mater. Des.*, 2017, **114**, 25–30.
5 A. Shah, Y. H. Wang, H. Huang, L. Zhang, D. X. Wang, L. Zhou, Y. P. Duan, X. L. Dong and Z. D. Zhang, *Compos. Struct.*, 2015, **131**, 1132–1141.
6 A. Shah, A. Ding, Y. H. Wang, L. Zhang, D. X. Wang, J. Muhammad, H. Huang, Y. P. Duan, X. L. Dong and Z. D. Zhang, *Carbon*, 2016, **96**, 987–997.
7 J. Y. He, H. Wang, H. L. Huang, X. D. Xu, M. W. Chen, Y. Wu, X. J. Liu, T. G. Nieh, K. An and Z. P. Lu, *Acta Mater.*, 2016, **102**, 187–196.
8 C. Y. Shang, E. Axinte, J. Sun, X. T. Li, P. Li, J. W. Du, P. C. Qiao and Y. Wang, *Mater. Des.*, 2017, **117**, 193–202.
9 A. J. Zhang, J. S. Han, B. Su, P. D. Li and J. H. Meng, *Mater. Des.*, 2017, **114**, 253–263.
10 J. M. Zhu, H. M. Fu, H. F. Zhang, A. M. Wang, H. Li and Z. Q. Hu, *Mater. Sci. Eng., A*, 2010, **527**, 7210–7214.
11 S. Praveen, B. Joysurya, K. Sanjay, K. G. Pradeep and S. K. Ravi, *Mater. Des.*, 2017, **134**, 426–433.
12 C. M. Lin and H. L. Tsai, *Intermetallics*, 2011, **19**, 288–294.
13 B. Schuh, F. Mendez-Martin, B. Völker, E. P. George, H. Clemens, R. Pippan and A. Hohenwarter, *Acta Mater.*, 2015, **96**, 258–268.
14 H. P. Chou, Y. S. Chang, S. K. Chen and J. W. Yeh, *Mater. Sci. Eng., B*, 2009, **163**, 184–189.
15 D. H. Xiao, P. F. Zhou, W. Q. Wu, H. Y. Diao, M. C. Gao, M. Song and P. K. Liaw, *Mater. Des.*, 2017, **116**, 438–447.
16 J. W. Yeh, S. K. Chen, S. J. Lin, J. Y. Gan and T. S. Chin, *Adv. Eng. Mater.*, 2004, **6**, 299–303.
17 J. Y. He, W. H. Liu, H. Wang, Y. Wu, X. J. Liu, T. G. Nieh and Z. P. Lu, *Acta Mater.*, 2014, **62**, 105–113.
18 X. Yang and Y. Zhang, *Mater. Chem. Phys.*, 2012, **132**, 233–238.
19 S. Guo and C. T. Liu, *Prog. Nat. Sci.: Mater. Int.*, 2011, **21**, 433–446.
20 R. Raghavan, K. C. Hari Kumar and B. S. Murty, *J. Alloys Compd.*, 2012, **544**, 152–158.
21 Y. J. Zhao, J. W. Qiao, S. G. Ma, M. C. Gao, H. J. Yang, M. W. Chen and Y. Zhang, *Mater. Des.*, 2016, **96**, 10–15.
22 Y. Zhang, T. T. Zuo, Y. Q. Cheng and K. L. Peter, *Sci. Rep.*, 2013, **3**, 1455.
23 B. Y. Wu, W. P. Chen, Z. F. Jiang, Z. Chen and Z. Q. Fu, *Mater. Sci. Eng., A*, 2016, **676**, 492–500.
24 M. Vaidya, S. Trubel, B. S. Murty, G. Wilde and S. V. Divinski, *J. Alloys Compd.*, 2016, **688**, 994–1001.

25 C. P. Lee, C. C. Chang, Y. Y. Chen, J. W. Yeh and H. C. Shih, *Corros. Sci.*, 2008, **50**, 2053–2060.

26 C. M. Liu, H. M. Wang, S. Q. Zhang, H. B. Tang and A. L. Zhang, *J. Alloys Compd.*, 2014, **583**, 162–169.

27 Q. Zhang, H. Xu, X. H. Tan, X. L. Hou, S. W. Wu, G. S. Tan and L. Y. Yu, *J. Alloys Compd.*, 2017, **693**, 1061–1067.

28 P. P. Yang, Y. Liu, X. C. Zhao, J. W. Cheng and H. Li, *Adv. Powder Technol.*, 2016, **27**, 1128–1133.

29 P. P. Yang, Y. Liu, X. C. Zhao, J. W. Cheng and H. Li, *J. Mater. Res.*, 2016, **31**, 2398–2406.

30 H. G. Yu, X. Huang, P. Wang and J. G. Yu, *J. Phys. Chem. C*, 2016, **120**, 3722–3730.

31 D. Lang, F. Y. Cheng and Q. J. Xiang, *Catal. Sci. Technol.*, 2016, **6**, 6207–6216.

32 K. L. He, J. Xie, Z. H. Yang, R. C. Shen, Y. P. Fang, S. Ma, X. B. Chen and X. Li, *Catal. Sci. Technol.*, 2017, **7**, 1193–1202.

33 M. G. Han, D. F. Liang, J. L. Xie and L. J. Deng, *J. Appl. Phys.*, 2012, **111**, 07A317.

34 M. G. Han and L. J. Deng, *J. Magn. Magn. Mater.*, 2013, **337–338**, 70–73.

35 Z. Q. Zhang, J. Q. Wei, W. F. Yang, L. Qiao, T. Wang and F. Li, *Physica B: Condens. Matter.*, 2011, **406**, 3896–3900.

36 Y. B. Feng, C. M. Tang and T. Qiu, *Mater. Sci. Eng., B*, 2013, **178**, 1005–1011.

37 Y. H. Wu, M. G. Han, T. Liu and L. J. Deng, *J. Appl. Phys.*, 2015, **118**, 023902.

38 L. L. Song, Y. P. Duan, Y. H. Zhang and T. M. Wang, *Comput. Mater. Sci.*, 2017, **138**, 288–294.

39 Y. P. Duan, Z. Liu, Y. H. Zhang and M. Wen, *J. Mater. Chem. C*, 2013, **1**, 1990–1994.

40 Y. H. Wu, M. G. Han, Z. K. Tang and L. J. Deng, *J. Appl. Phys.*, 2014, **115**, 163902.

41 G. Li, Y. Cui, N. Zhang, X. Wang and J. L. Xie, *Physica B: Condens. Matter.*, 2016, **481**, 1–7.

42 Y. P. Duan, Y. H. Zhang, T. M. Wang, S. C. Gu, X. Li and X. J. Lv, *Mater. Sci. Eng., B*, 2014, **185**, 86–93.

43 Y. P. Duan, S. C. Gu, Z. L. Zhang and M. Wen, *J. Alloys Compd.*, 2012, **542**, 90–96.